Giant, 26, 2025, 100380

Full-length article

Lanthanum-substituted CaMo-MOF via controlled metal nitrate ratios for Electrochemical Performance

P. Arularasan[a], Mohd Arif Dar[b,g,*], Mohammad Rezaul Karim[c], P Rajesh[d], M Pavithra[e], Sambasivam Sangaraju[f,*]

[a] Department of Physics, Dwaraka Doss Goverdhan Doss Vaishnav College, Chennai, Tamil Nadu 600107, India
[b] Institute of Power Engineering, Universiti Tenaga Nasional, Jalan IKRAM-UNITEN, Kajang, Selangor-43000, Malaysia
[c] Center of Excellence for Research in Engineering Materials (CEREM), Deanship of Scientific Research, College of Engineering, King Saud University, Riyadh 11421, Saudi Arabia
[d] Department of Physics, School of Basic Science, Vels Institute of Science and Technology & Advanced Studies, Pallavaram, Chennai, Tamil Nadu 600117, India
[e] Department of Condensed Matter Physics, Saveetha School of Engineering, Saveetha Institute of Medical and Technical Sciences (SIMATS), Chennai, Tamil Nadu-602105, India
[f] National Water and Energy Center, United Arab Emirates University, Al Ain 15551, United Arab Emirates
[g] Faculty of Allied Health Sciences, Chettinad Hospital, and Research Institute, Chettinad Academy of Research and Education, Kelambakkam-603103, Tamil Nadu, India

Keywords: Precipitation method, Tetragonal scheelite-type structure, Electrochemical analysis

In this study, a series of $La_xCa_{1-x}Mo$-based metal-organic frameworks (MOFs), designated as CML1, CML2, CML3 and CML4, were synthesized via a controlled precipitation method. A comprehensive characterization was performed using X-ray diffraction (XRD), Fourier transform infrared spectroscopy (FTIR), Raman spectroscopy and X-ray photoelectron spectroscopy (XPS). The XRD confirmed the formation of a single-phase tetragonal scheelite-type structure ($I4_1/a$), with no secondary phases detected. The average crystallite size is found to be 54, 52, 42 and 16 (nm) in CML1, CML2, CML3 and CML4 MOFs. The SEM reveals a morphological evolution from irregular granules in CML1 to well-faceted rods in CML4 MOFs. The electrochemical analysis revealed a clear performance hierarchy, with CML3 electrode exhibiting the highest the specific capacitance in a two-electrode system. The coulombic efficiency of 96 % is retained by the CML3 electrode even after 1000 GCD cycles in a two-electrode system.

1 Introduction

MOFs represent an expansive class of crystalline hybrid materials constructed from metal nodes or clusters coordinated with multidentate organic linkers. Due to their high surface area, adjustable pore size, structural tunability, and multifunctional chemistry, MOFs have found widespread application in gas separation, drug delivery, catalysis and energy storage technologies [1]. Their unique architecture facilitates the rational integration of electroactive components into highly porous structures, making them attractive for electrochemical energy storage devices such as supercapacitors and batteries. In supercapacitors, MOFs enable surface-driven charge accumulation via electric double-layer capacitance and on the other hand, depending on the metal centre, they can also contribute pseudocapacitive behaviour through faradaic redox reactions.

* Corresponding authors.
E-mail addresses: dararifphy@gmail.com (M.A. Dar), s_sambasivam@uaeu.ac.ae (S. Sangaraju).
Received 26 August 2025; Received in revised form 22 October 2025; Accepted 27 October 2025

https://doi.org/10.1016/j.giant.2025.100380

Furthermore, their ability to accommodate alkali and multivalent ions within a stable lattice has rendered them viable hosts in lithium-ion and emerging sodium- or calcium-ion batteries [2–4]. In addition to energy storage, MOFs have shown strong potential in environmental energy technologies such as CO_2 capture and gas storage. Their open metal coordination sites and high surface-to-volume ratios facilitate both physisorption and chemisorption of gas molecules with high selectivity and capacity [5].

MOFs can also be functionalized with catalytic centres, such as lanthanides or transition metals, and have been developed for CO_2 conversion reactions, including hydrogenation to formate and cycloaddition to produce cyclic carbonates, thereby expanding their utility in carbon-neutral energy cycles [6]. Among the many MOF systems, calcium-based MOFs (Ca-MOFs) have recently attracted attention due to the natural abundance, low toxicity, and favourable coordination chemistry of calcium. The divalent nature of calcium enables the formation of stable carboxylate-based frameworks with relatively large pore sizes and good aqueous stability, offering an eco-friendly platform for scalable MOF development. However, like many alkaline earth MOFs, Ca-MOFs often suffer from limited electrical conductivity and poor electrochemical activity, necessitating chemical modification strategies to enhance their performance in energy-related applications [7,8]. A promising strategy to address these limitations is the isovalent or aliovalent substitution of metal centers, among which lanthanum (La^{3+}) has shown particular promise. As a trivalent rare-earth ion, La^{3+} has a relatively large ionic radius (1.16 Å) compared to Ca^{2+} (0.99 Å), Mg^{2+} (0.72 Å), or transition metals like Ni^{2+} (0.69 Å). This difference can significantly influence crystal field geometry, bonding angles, and framework flexibility, resulting in pore size modulation and structural distortion within the MOF lattice [9]. The ionic size mismatch introduces local strain and may alter the symmetry of coordination polyhedra, often expanding lattice parameters, a feature favourable for ion mobility and electrolyte accessibility, which are both crucial for electrochemical energy storage. However, excessive or uncontrolled substitution may destabilize the framework, reduce crystallinity, or induce amorphous phase formation, underscoring the importance of optimizing metal ratios [10].

Although La^{3+} is generally considered redox-inactive due to its stable +3 oxidation state, its incorporation into MOFs can profoundly influence their electrochemical behavior and overall functional properties. The La^{3+} does not directly participating in redox reactions but contributes indirectly by modifying the structural, electronic, and defect characteristics of the framework. The substitution of La^{3+} into the lattice often leads to the generation of intrinsic defects such as oxygen vacancies, missing linker sites, or charge-compensating proton losses. These structural imperfections create localized energy states within the band gap, improving electronic conductivity and facilitating rapid charge transfer across the electrode–electrolyte interface. Additionally, the introduction of La^{3+} ions can lower the activation barrier for ionic diffusion, thereby enhancing ion mobility and rate capability, which are essential for high-performance energy storage applications [11]. Further, La^{3+} doping exerts a pronounced influence on the crystal field environment and local coordination geometry. Such changes can alter the electronic band alignment, modulate charge density distribution, and optimize carrier transport pathways. The presence of La^{3+} also tends to stabilize the framework by strengthening metal-oxygen coordination bonds, improving thermal and chemical stability under electrochemical cycling conditions [12]. The incorporation of La^{3+} into Ca-MOFs introduces dual-metal coordination sites that synergistically enhance redox activity and ion adsorption dynamics. The resulting heterometallic interaction promotes efficient charge separation and facilitates reversible electrochemical reactions. These structural and electronic modifications collectively contribute to superior pseudocapacitive behavior, improved hydrophilicity, enhanced solvent compatibility, and optimized charge storage efficiency, making La-modified Ca-MOFs promising candidates for advanced energy storage devices [13].

Metal substitution in MOFs has emerged as an effective strategy to tailor their structural properties, electronic structure and functional behaviour. The transition-metal doping has been widely explored for improving conductivity, redox activity and electrocatalytic efficiency, however, the role of lanthanum incorporation in alkaline earth metal frameworks, particularly Ca-based MOFs, remains largely unexplored. In this study, La-substituted Ca-MOFs were synthesized through a precisely controlled co-precipitation route using calcium and lanthanum nitrates at varying molar ratios to achieve uniform cation distribution and compositional tuning. The resulting materials, designated as CML1, CML2, CML3, and CML4, were systematically characterized using XRD, SEM, TEM, and BET techniques to examine their crystalline structure, morphology and surface textural properties. Subsequently, the corresponding electrodes were fabricated to evaluate their electrochemical characteristics and to elucidate the influence of La incorporation on charge storage behaviour, ion diffusion dynamics and electrical conductivity. This work establishes a novel framework for understanding how La substitution modulates the electrochemical properties of Ca-MOFs, thereby providing a pathway for designing high-performance materials for next-generation energy storage applications.

2 Experimental section

2.1 Materials

Calcium nitrate tetrahydrate [$Ca(NO_3)_2{\cdot}4H_2O$], lanthanum nitrate hexahydrate [$La(NO_3)_3{\cdot}6H_2O$], sodium molybdate dihydrate [$Na_2MoO_4{\cdot}2H_2O$], and 2-methylimidazole ($C_4H_6N_2$) were obtained from Sigma Aldrich and used as received without further purification. Distilled water and ethanol were purchased from Hyma Chemicals and used as solvents.

2.2 Synthesis of La_xCaMo_{1-x} MOF

A series of $La_xCa_{1-x}Mo$ MOFs was synthesized via a controlled precipitation method by systematically varying the La:Mo molar ratios. In each synthesis, a predetermined amount of calcium nitrate tetrahydrate was dissolved in 25 mL of distilled water under continuous stirring to achieve complete dissolution. Lanthanum nitrate hexahydrate was then added to this solution in varying amounts, corresponding to the desired La substitution levels

Table 1

Different ratios of Lanthanum nitrate and Calcium Nitrate.

Sample Code	$Ca(NO_3)_2{\cdot}4H_2O$ (M)	$[La(NO_3)_3]$ (M)
CML1	0.9 M	0.1 M
CML2	0.8 M	0.2 M
CML3	0.7 M	0.3 M
CML4	0.6 M	0.4 M

(detailed in Table 1), and the mixture was stirred further to achieve homogeneity. Separately, sodium molybdate dihydrate was dissolved in 25 ml of distilled water to form a clear solution, which was then added to the resultant solution under constant stirring. Upon addition, immediate precipitation occurred, indicating the formation of metal–molybdate complexes. Following this, a stoichiometric amount of 2-methylimidazole (solution in 50 ml of distilled water) was added to the mixture to act as the organic linker. The resulting suspension was stirred continuously at 60 °C for 2 h to promote crystallization and framework formation. The precipitated solids were collected by filtration, washed thoroughly with ethanol to remove uncoordinated species and dried overnight in a hot air oven at 80 °C. The materials were labelled CML1, CML2, CML3, and CML4 in order of increasing La^{3+} content (i.e., increasing x in $La_xCa_{1-x}Mo$).

2.3 Materials characterization

The phase purity of the synthesized materials was confirmed by XRD using a Bruker D8 diffractometer equipped with Cu-Kα radiation (λ = 1.514 Å). The FTIR spectra were recorded using a PerkinElmer spectrometer to identify functional groups. The Raman spectra were obtained using a Bruker RFS 27 spectrometer. The UV-Visible (JASCO UV VIS-V-730) was used for determining the absorbance, and for the TG/DTA (NETZSCH STA 449F3) instrument was utilized. The surface morphology and microstructure were examined using SEM (Zeiss Scanning Electron Microscope) and high-resolution transmission electron microscopy (HR-TEM, JEM-2100 Plus). The surface chemical composition and oxidation states of the elements were analysed using XPS (Thermo Fisher Scientific K-Alpha). The electrochemical studies were performed using Metrohm Autolab PGSTAT204.

2.4 Electrochemical setup and electrode preparation

In a standard three-electrode electrochemical setup, a platinum wire and an Ag/AgCl electrode were employed as the counter and reference electrodes, respectively. The working electrode was fabricated by homogenously blending the synthesized active material with polyvinylidene fluoride (PVDF) and acetylene black in a weight ratio of 80:10:10, using N-methyl-2-pyrrolidone (NMP) as the solvent to form a uniform slurry. This slurry was subsequently coated onto a pre-cleaned nickel foam substrate (2 × 1 cm²) and coin-sized graphite for a two-electrode setup. The electrodes are dried at 80 °C for 12 h to ensure solvent evaporation and electrode integrity. A 0.5 M aqueous KOH solution was used as the electrolyte for all electrochemical measurements. The mass loading of the active material on the electrode was maintained

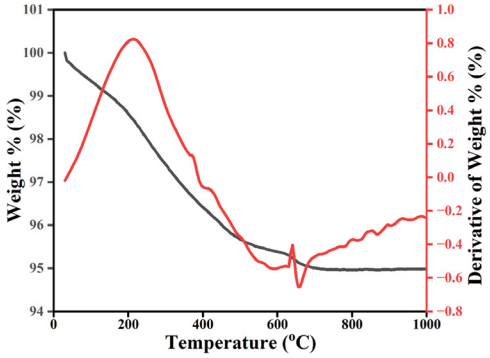

Fig. 1

TGA-DTA analysis of CML1 MOF.

at approximately 1–1.5 mg/cm² for Ni foam and 2–3 mg/cm² for graphite substrate.

3 Results and discussion

3.1 Thermal stability

To investigate the thermal strength of the synthesized LaCaMo-MOF, thermogravimetric analysis (TGA) and differential thermal analysis (DTA) were performed under a nitrogen atmosphere from room temperature to 1000 °C. The corresponding TGA/DTG curves of CML1 are shown in Fig. 1. The initial weight loss of ~1–2 % below 150 °C is attributed to the desorption of physiosorbed water and loosely bound solvent molecules. The DTG curve displays a mild endothermic peak in this region, which is consistent with physical evaporation without structural decomposition. In the second degradation step, extending from 150 to 500 °C, it involves a gradual mass loss of ~3 %, which is attributed to the stepwise removal of coordinated solvent molecules and partial decomposition of organic linkers. The absence of sharp DTG peaks in this region suggests overlapping low-energy degradation events or a continuous defragmentation of the MOF's ligand framework. A prominent DTA peak minimum at approximately 630 °C, accompanied by a sharp mass loss, signifies the breakdown of the MOF architecture, particularly the decarboxylation of the linker molecules and disruption of metal-ligand bonds. Beyond 700 °C, no significant weight loss is observed, indicating the formation of thermally stable inorganic residues, presumably La_2O_3, CaO, or mixed metal oxides, which are known to be stable under inert atmospheres at elevated temperatures [19]. The high residual mass (~95 %) further reflects the excellent char-forming ability of this MOF system, a favourable trait for applications.

3.2 Structural analysis

The phase purity and structure of the CML1, CML2, CML3 and CML4 MOFs were investigated using XRD spectra (Fig. 2). The diffraction peaks are located at 2θ = 18.04°, 28.83°, 31.52°, 34.52°, 39.59°, 47.21°, 49.30°, 54.30°, 58.26°, 59.61°, 75.82°, 79.41°, 80.68°, 82.39° and 85.61° corresponding to the (101), (112), (004), (200), (211), (204), (220), (116), (303), (224), (208), (332), (307), (420) and (334) hkl planes, respectively. The observed peaks match closely with the reference pattern for synthetic Powellite

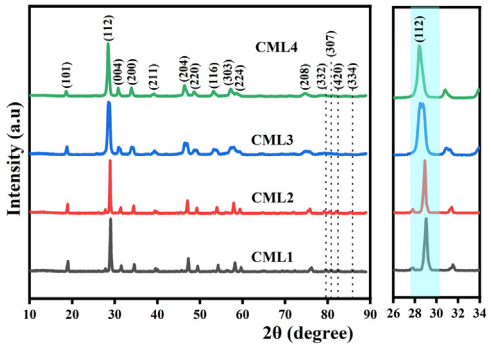

Fig. 2

XRD spectra of the CML1, CML2, CML3, and CML4 MOFs.

($CaMoO_4$), which is indexed to the tetragonal crystal system with space group $I4_1/a$ (PDF No. 01–077–2238) (JCPDS card no. 29–0351) [14]. Notably, the absence of any secondary reflections confirms the single-phase nature of all samples and indicates that La^{3+} has been successfully incorporated into the $CaMoO_4$ lattice without forming any discrete phases like $La_2(MoO_4)_3$ or $LaMoO_4$. The average crystallite size was calculated using Debye-Scherrer equation.

$$D = \frac{K\lambda}{\beta\cos\theta} \quad (1)$$

where D is the average crystallite size, $K = 0.9$ is the shape factor, $\lambda = 1.5406$ Å is the X-ray wavelength, β is the full width at half maximum (FWHM) in radians, and θ is the Bragg angle. The average crystallite size of the CML1, CML2, CML and CML4 is 54, 52, 42 and 16 (nm), suggesting that La^{3+} incorporation into CaMo. The ionic radius of La^{3+} (1.16 Å) is slightly larger than that of Ca^{2+} (app. 1.0 Å). Thus, La^{3+} substitution at the Ca^{2+} site induces slight lattice relaxation that minimizes strain, enhances structural stability and facilitates controlled nucleation, leading to the formation of larger, well-ordered crystallites. The magnified XRD window between 26° and 34° (Fig. 2) reveals subtle variations in peak intensity and a widening of the peaks with increasing La content, indicative of enhanced crystallinity. Moreover, there is a slight shift of peaks towards lower theta values from CML1 to CML4 MOFs, implying that La^{3+} substitutes into the Ca^{2+} sites without significant distortion of the unit cell. However, the increase in peak sharpness and symmetry reflects reduced microstrain and defect density at higher Lanthanum ion substitution.

To analyze the surface chemical composition and oxidation states of the elements present in the CML1, CML2, CML3 and CML4 MOFs, the XPS studies were done for the CML1 MOF. The survey scan confirms the presence of Ca, Mo, La, and O (Fig. 3a). Fig. 3b shows the deconvolution curves of Ca 2p spectra, where two well-defined peaks are observed at binding energies of

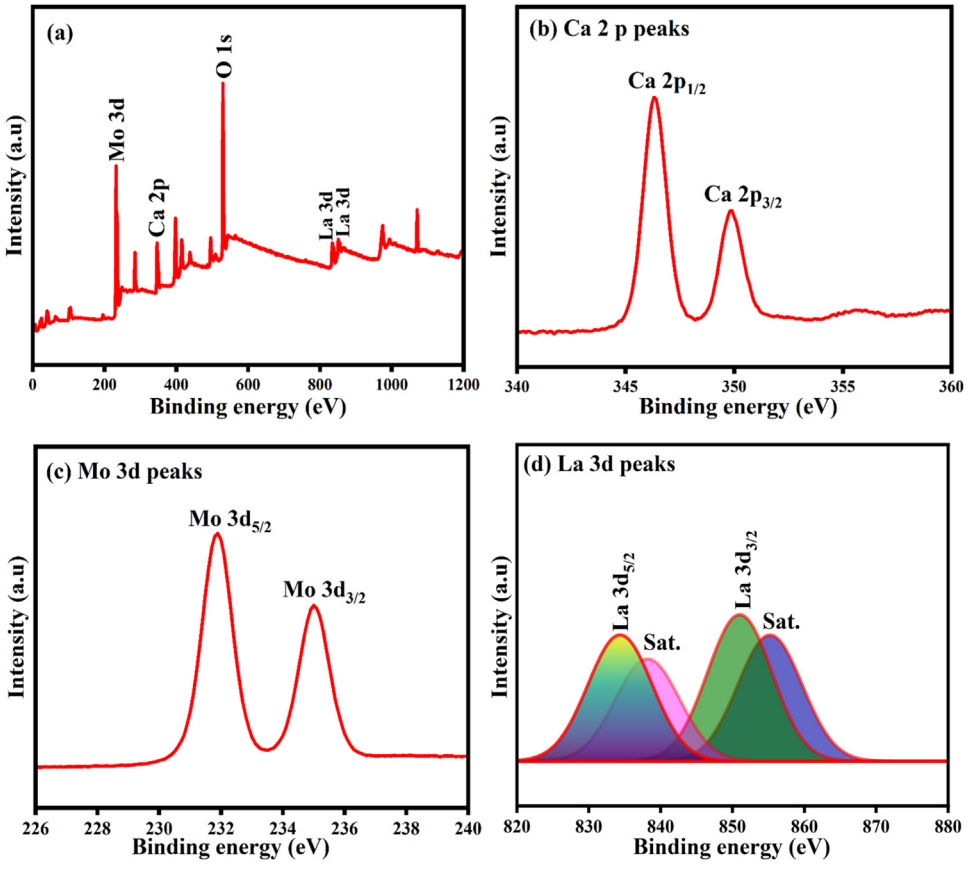

Fig. 3

(a) XPS survey spectra (b) Ca 2p peaks (c) Mo 3d peaks and (d) La 3d peaks of the CML1 MOF.

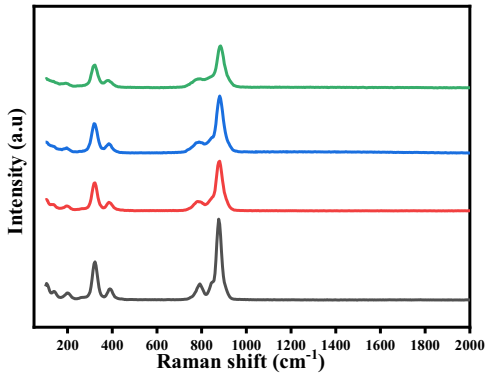

Fig. 4

Raman spectra of CML1, CML2, CML3, and CML4 MOFs.

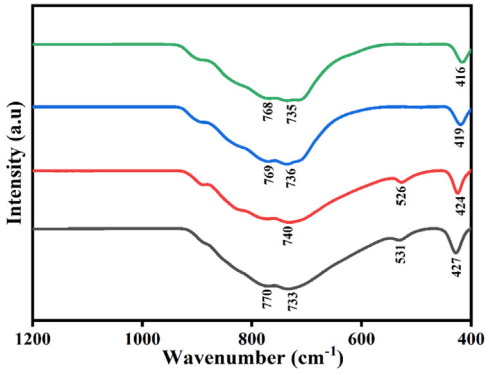

Fig. 5

FTIR spectra of the CML1, CML2, CML3, and CML4 MOFs.

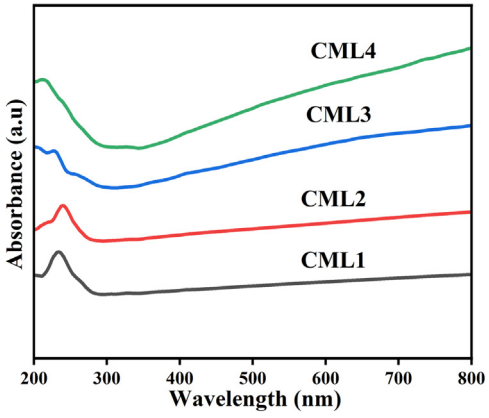

Fig. 6

UV-Vis absorbance spectra of the CML1, CML2, CML3, and CML4 MOFs.

approximately 346.5 eV and 350.1 eV, corresponding to Ca $2p_{1/2}$ and Ca $2p_{3/2}$, respectively [15]. Fig. 3c shows the deconvolution curves of the Mo 3d peaks at 232.5 eV and 235.6 eV, assigned to Mo $3d_{5/2}$ and Mo $3d_{3/2}$, respectively. These binding energies are characteristic of the Mo^{6+} oxidation state, indicating that molybdenum exists primarily as MoO_4^{2-} within the lattice, and no evidence of lower oxidation states (Mo^{5+} or Mo^{4+}) is observed [16]. Fig. 3d displays the deconvolution spectra of the La 3d peaks observed between binding energies of 820–870 eV. The peaks are observed at 835.6 eV (La $3d_{5/2}$) and 852.5 eV (La $3d_{3/2}$). The presence of two satellite peaks further validates the La^{3+} oxidation state and suggests strong hybridization between La 4f and O 2p orbitals [17]. The XPS analysis confirms the successful formation of a La-substituted $CaMoO_4$-type structure with the expected oxidation states of Ca^{2+}, Mo^{6+} and La^{3+}. This confirms the doping of La in the CaMo MOFs.

3.3 Raman analysis

Fig. 4 shows the Raman spectra of the CML1, CML2, CML3 and CML4 MOFs. The spectra show major peaks at 199, 320, 388, 791 and 877 (cm^{-1}). The peaks observed at 320 and 877 (cm^{-1}) belong to the Ag active modes and the bands observed at 199, 388 and 791 (cm^{-1}) belong to the Eg active modes, confirming the integrity of the MoO_4^{2-} tetrahedra [18]. All these bands show a slight shift from CML1 to CML4 MOFs due to the incorporation of La ions into the Ca ions. Further, the small bands observed below 150 cm^{-1} correspond to the Ca^{2+} cations [19].

3.4 FTIR analysis

FTIR spectroscopy was performed to investigate the functional groups and bonding of the CML1, CML2, CML3 and CML4 MOFs.Fig. 5 shows the FTIR spectra of the CML1, CML2, CML3 and CML4 MOFs. The three main peaks are consistent from CML1 to CML4 MOFs, observed at 427, 733 and 770 (cm^{-1}). The absorption bands at 733 and 770 (cm^{-1}) are assigned to the antisymmetric stretching vibration of the Mo-O bond in the $(MoO_4)^{2-}$ tetrahedra, while the band at 427 cm^{-1} corresponds to Ca-O vibrations [20,21]. The shifting and intensity changes of these three main FTIR peaks from CML1 to CML4 MOFs confirm the incorporation of La^{3+} ions into the $CaMoO_4$ lattice without altering the fundamental structure. . Furthermore, the band observed around 531 cm^{-1} in LCM1 and LCM2 MOFs may be raised due to the doping of La ions.

3.5 UV–Visible analysis

UV–Visible absorption spectroscopy was employed to investigate the optical properties and electronic structure of the CML1, CML2, CML3, and CML4 MOFs. The absorption spectra recorded in the 200–800 nm range are shown in Fig. 6. All samples exhibit strong absorption in the UV region, which is typical for molybdate-based materials due to charge-transfer transitions between oxygen 2p and molybdenum 4d orbitals. The absorption edge for CML1 appears near 250 nm, attributed to the $O^{2-} \rightarrow Mo^{6+}$ ligand-to-metal charge transfer (LMCT) [22]. As La^{3+} content increases from CML1 to CML4, the absorption edge systematically shifts toward higher wavelengths, indicating a reduction in the optical band gap. This shift may be ascribed to local lattice distortion and electronic structure modification introduced by the substitution of Ca^{2+} with La^{3+} ions. The broadening of absorption profiles and increasing absorbance with La^{3+} content suggest improved light-harvesting ability and enhanced defect-related sub-band states, which could influence the electrochemical or optoelectronic properties of the materials.

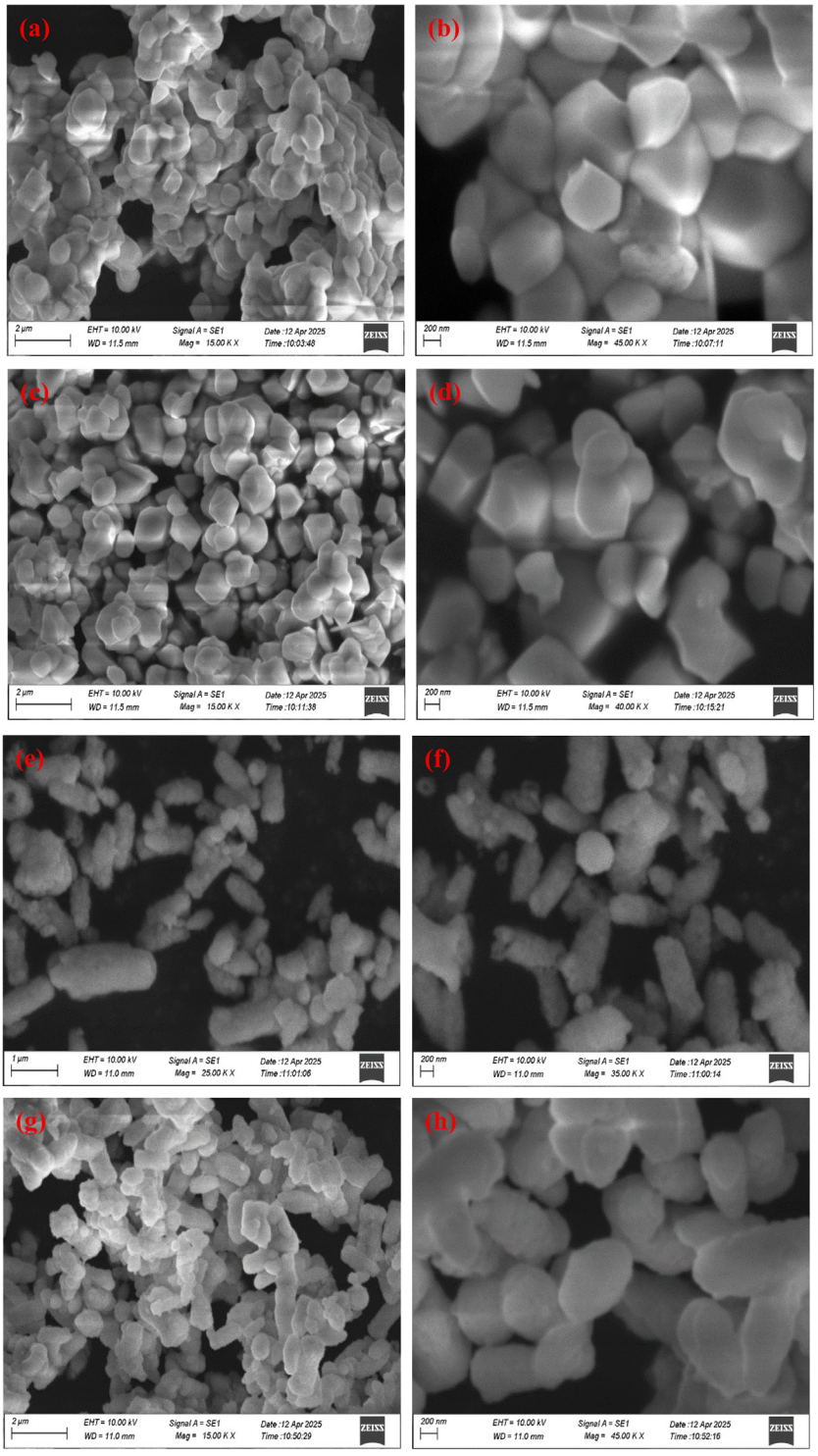

Fig. 7

SEM images of the (a, b) CML1, (c, d) CML2 (e, f) CML3 and (g, h) CML4 MOFs.

3.6 Morphological analysis

Fig. 7 shows SEM Images of CML1, CML2, CML3, and CML4 MOFs. The SEM studies were employed to analyze the surface morphology, particle shape and size distribution of the CML1, CML2, CML3 and CML4 MOF. Figs. 7 (a, b) show the SEM images of the CML1 MOF. For CML1 Fig. 7 (a, b), the particles appear as agglomerated irregular granules with spherical/polygonal-like morphology. Fig. 7 (c, d) show the SEM images of the CML2 MOF. Here, more uniform grain distribution with better-defined faceted structures is seen in CML2 MOF. The particles are slightly larger and more angular compared to CML1 MOF. Fig. 7 (e, f) shows the SEM images of the CML3 MOF. Here, the particles evolve into well-

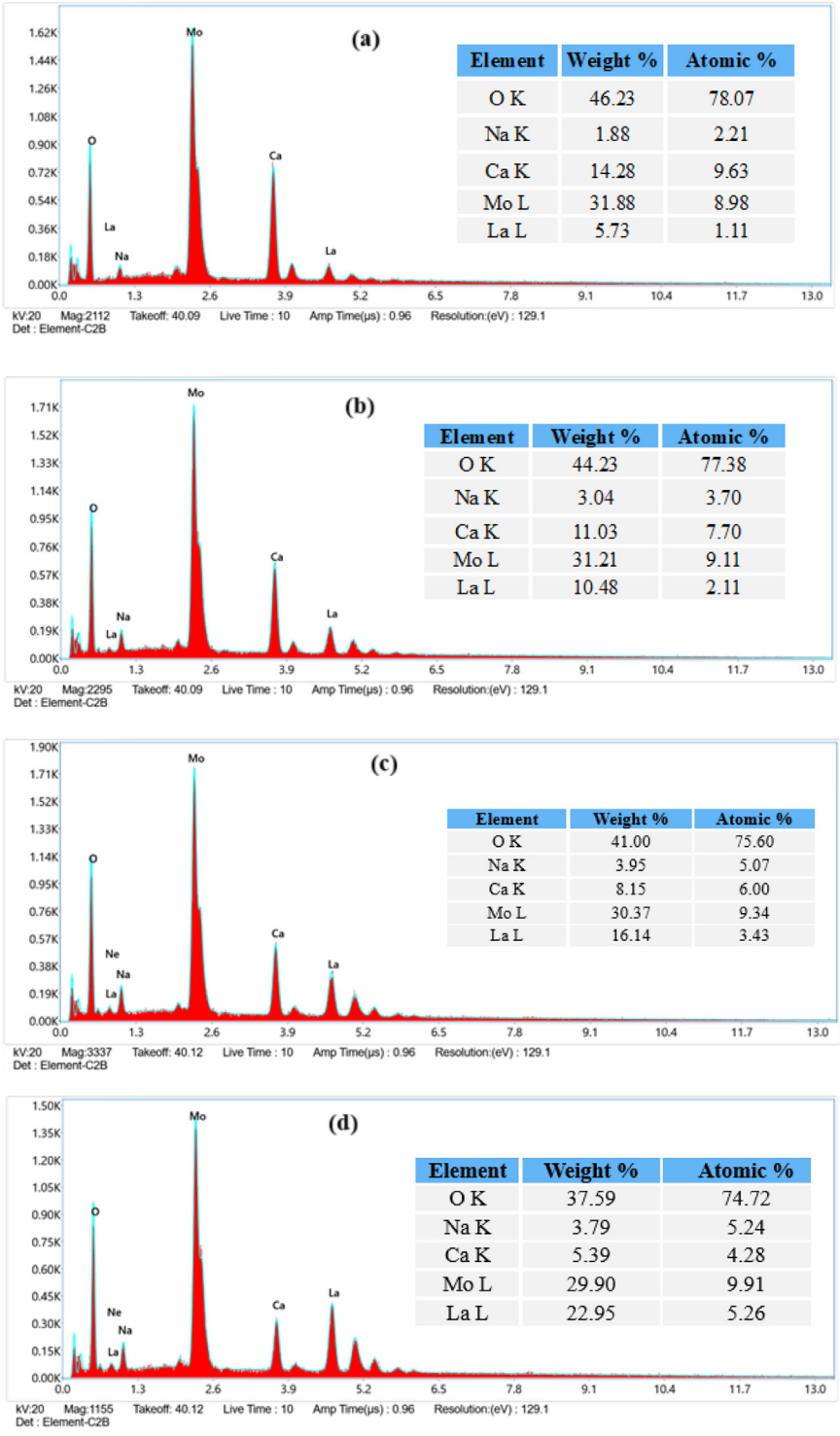

Fig. 8

EDX spectra of the (a) CML1, (b) CML2, (c) CML3, and (d) CML4 MOFs.

formed rod-like or elongated morphologies. Fig. 7 (g, h) shows the SEM images of the CML4 MOF. Here, oval structures are observed. The change in morphology from CML1 to CML4 MOF implies enhanced structural reorganization and improved particle packing with increasing La^{3+} content.

Energy Dispersive X-ray Spectroscopy (EDX) was performed in conjunction with SEM to determine the elemental composition of the synthesized CML1, CML2, CML3 and CML4 MOFs. The representative EDX spectra are shown in Fig. 8 (a-d) for CML1, CML2, CML3 andCML4 MOFs, respectively. For CML1 Fig. 8a

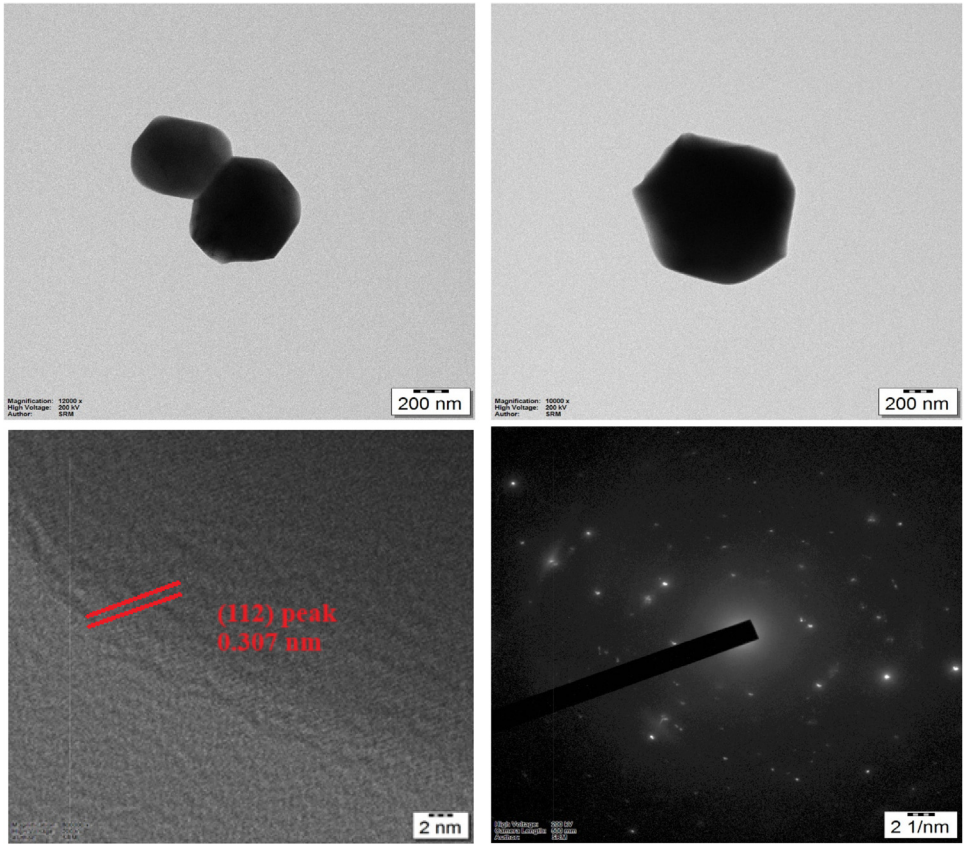

Fig. 9

(a, b) TEM images (c) HRTEM image and (d) SAED image of CML1 MOF.

the distinct peaks corresponding to Mo, Ca, O, and minor Na are observed, confirming the expected stoichiometry of $CaMoO_4$. A low-intensity La peak observed can be attributed to the incorporation of La^{3+} ions in the lattice of CaMo. In CML2 Fig. 8b, the intensity of the La peak increases, accompanied by a slight reduction in the Ca signal, which can be ascribed to the partial substitution of Ca^{2+} by La^{3+}. Moreover, Mo remains as a dominant element, confirming the structural integrity of the molybdate framework. Fig. 8c further demonstrates the progressive increase in La content with a corresponding decline in Ca signal. The intensity of the Mo peak remains nearly unchanged, reaffirming the fixed Mo from CML1 to CML4 MOFs. Finally, CML4 Fig. 8d shows a significant La peak, which is indicative of higher doping levels. The Ca peak is the weakest in this sample, supporting the successful substitution of Ca^{2+} ions by La^{3+} ions to the greatest extent among the series. These results strongly support the findings from XRD, FTIR, and XPS, reinforcing the phase purity and chemical integrity of the synthesized materials.

Further, TEM/SAED analyses were carried out to examine the particle morphology, crystallinity, and lattice structure of the CML1, CML2, CML3 and CML4 MOFs. Fig. 9 (a, b) shows the TEM images of the CML1 MOF. The TEM images reveal well-defined, faceted particles with predominantly polygonal shapes, suggesting high crystallinity and anisotropic growth. The particles appear relatively uniform in size and the sharp edges and flat facets indicate a well-developed crystallates, consistent with scheelite-type molybdate morphologies observed in SEM. Fig. 9c shows the High-resolution transmission electron microscopy (HRTEM) image of the CML1 MOF reveals clear lattice fringes, indicative of long-range crystalline order. The interplanar spacing measured from the fringes is consistent with the (112) plane of tetragonal $CaMoO_4$ (d = 3.07 Å), supported by XRD analysis. The corresponding SAED pattern (Fig. 9d) exhibits a well-defined ring structure composed of discrete bright spots determines the crystalline nature of the synthesized MOFs. These findings are consistent with the structural and morphological information obtained from XRD and SEM, further validating the phase-purity and crystalline nature of the synthesized MOFs.

4 Electrochemical analysis

Fig. 10 (a-d) presents the CV curves of the CML1, CML2, CML3 and CML4 electrodes in a three-electrode system over a scan rate range of 10–100 mV/s^{-1}. All the electrodes exhibit quasi-rectangular-shaped CV profiles with distinguishable redox peaks, which signify a predominant pseudocapacitive charge storage behaviour governed by fast and reversible surface or near-surface faradaic redox reactions [23]. This characteristic is commonly observed in transition metal-based MOFs, where redox-active centres contribute significantly to energy storage via interfacial charge transfer [23,24]. As the scan rate increases, a progressive enhancement in current response is observed from all the samples, affirming their good rate capability

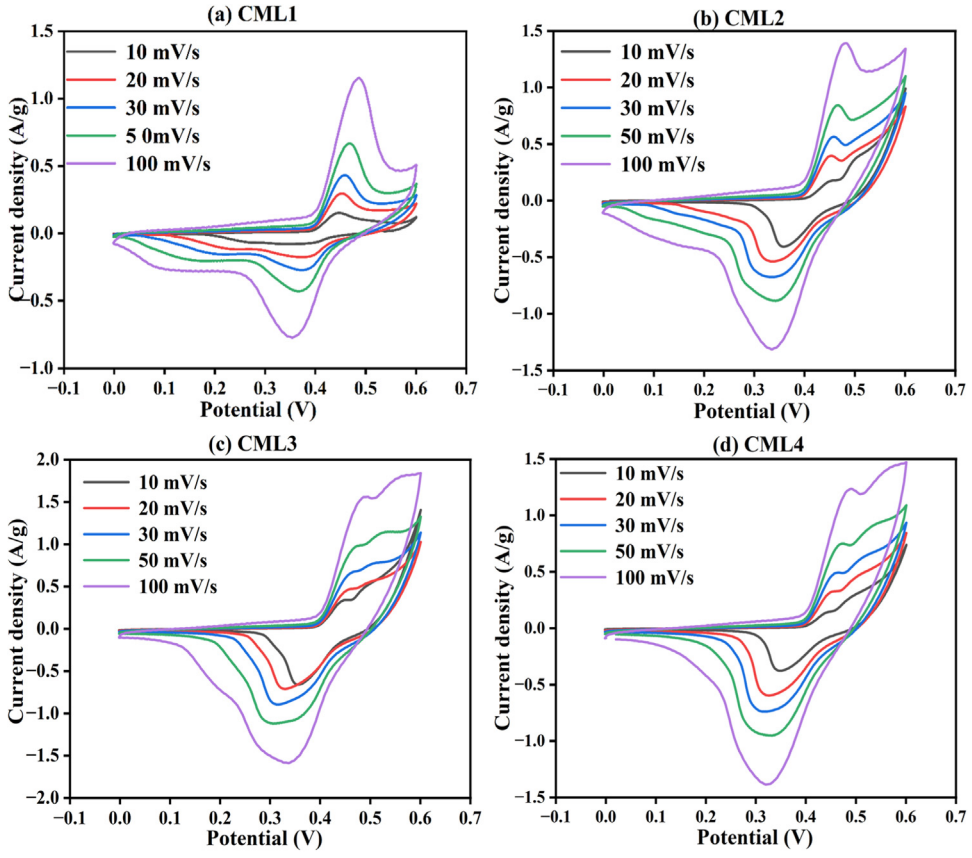

Fig. 10

CV curves of (a) CML1, (b) CML2, (c) CML3 and (d) CML4 electrodes in a three-electrode system.

and rapid ion diffusion kinetics. Notably, the CML3 electrode demonstrates the highest current density throughout the scan range, with clearly defined redox peaks and minimal potential separation, indicating superior electrochemical reversibility, fast charge-transfer kinetics, and low internal resistance. In contrast, the CML1, CML2 and CML4 electrodes display moderately symmetric CV curves with appreciable redox activity, suggesting partially effective La incorporation that supports improved but suboptimal electrochemical behaviour. Further, the charge storage mechanism of CML1, CML2, CML3, and CML4 electrodes was analysed using the Trasatti method to distinguish between capacitive and diffusion-controlled contributions. The Trasatti method involves evaluating the relationship between specific capacitance and scan rate. The total specific capacitance (C_T) was calculated from Fig. 11 (a, b). The y-intercept of the plot specific capacitance versus the inverse square root of the scan rate represents the intrinsic capacitance (C_o), while the y-intercept of the plot of inverse specific capacitance versus the square root of the scan rate corresponds to the total capacitance (C_T) for the CML1, CML2, CML3, and CML4 electrodes. Thus, the diffusion contribution of the specific capacitance (Ci) can be calculated using the equation given below.

$$C_T = C_i + C_o \quad (2)$$

The calculated values of C_T, C_i and C_o are given in Table 2. Finally, the percentage of diffusion-controlled contribution for

Table 2

C_o, C_T and C_i values of the CML1, CML2, CML3 and CML4 electrodes.

Sample electrode	C_o	C_T	C_i
CML1	5.52	55.00	49.48
CML2	12.70	56.43	43.73
CML3	28.14	60.06	31.92
CML4	11.30	56.92	45.64

CML1, CML2, CML3, and CML4 electrodes is illustrated in Fig. 12(a). The observed transition in charge storage mechanism from pseudocapacitive to EDLC behaviour from CML1 to CML3 electrodes can be attributed to the progressive incorporation of La^{3+} ions into the CaMo framework, which modulates both the electronic structure and surface characteristics of the material. As the La^{3+} content increases, the electrical conductivity and surface defect density are enhanced, facilitating faster ion transport and charge accumulation at the electrode/electrolyte interface, characteristics typical of EDLC behaviour. Additionally, the increased La substitution can lead to a more stable and less redox-active surface, thereby suppressing faradaic reactions and promoting non-faradaic charge storage. However, in the case of the CML4 electrode, the dominant pseudocapacitive behaviour may arise due to excessive La incorporation, which can distort

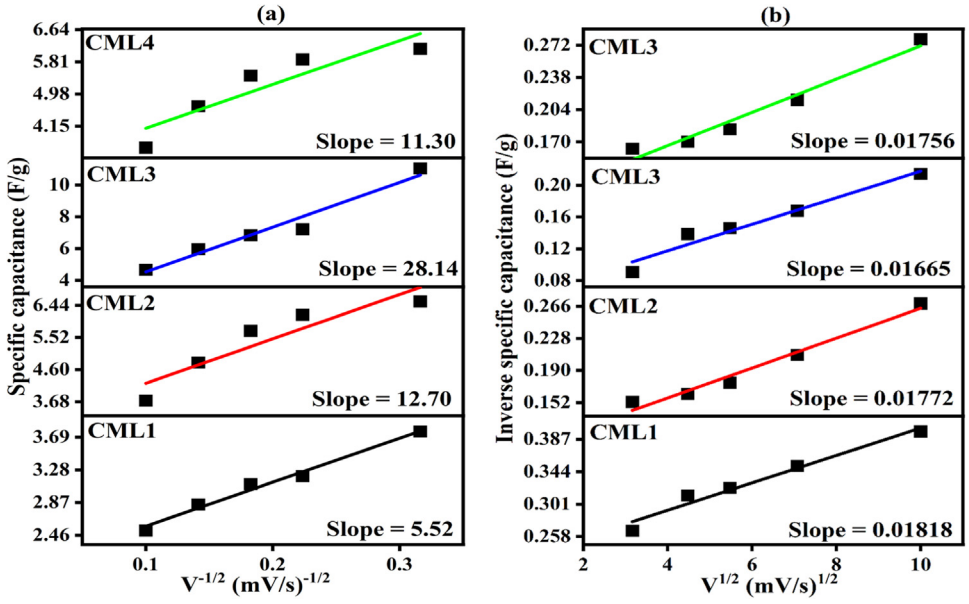

Fig. 11

(a) Inverse square root of scan rate versus specific capacitance (b) Square root of scan rate versus inverse specific capacitance of the CML1, CML2, CML3 and CML4 electrodes.

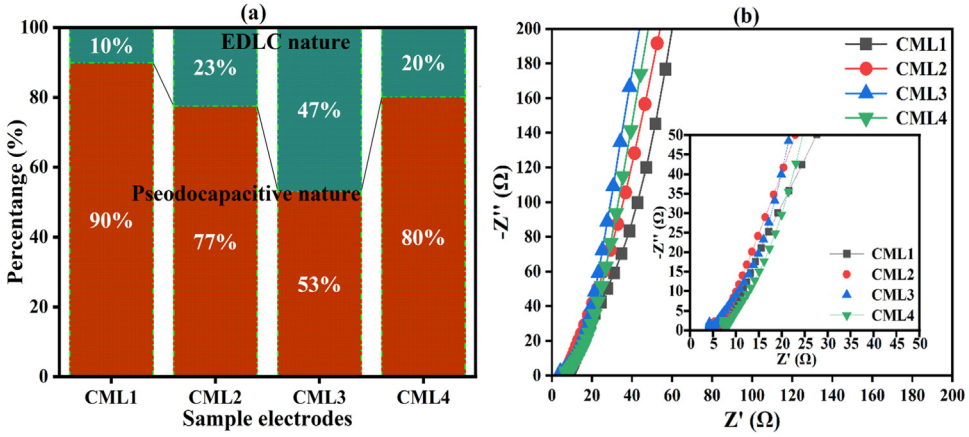

Fig. 12

(a) Capacitive contribution (b) Nyquist plot of the CML1, CML2, CML3, and CML4 electrodes in a three-electrode system.

the crystal lattice and introduce localized defect sites or oxygen vacancies. These defects act as active redox centers, enhancing faradaic charge transfer processes. Consequently, CML4 exhibits a higher contribution from pseudocapacitive reactions compared to the more EDLC-dominated CML3 electrode. Fig. 12(b) shows the Nyquist plots of the CML1, CML2, CML3 and CML4 electrodes. The Nyquist plot provides further insights into the charge transfer resistance and ion diffusion behaviour of CML1, CML2, CML3, and CML4 electrodes electrodes. The semicircle in the high-frequency region corresponds to the charge transfer resistance (Rct), while the low-frequency linear tail relates to Warburg impedance (diffusion resistance). The CML3 electrode exhibits the smallest semicircle and steepest tail, signifying the lowest Rct and superior ion transport behaviour. These results are consistent with the CV performance. Further, the increase in the contribution of EDLC nature can also be seen in the CV curves of the two-electrode system.

To check out further insights into the electrode performance, a two-electrode cell was made for the CML1, CML2 and CML3 electrodes separately (acting as cathode), in which the AC electrode acts as anode, separated by a glass microfibre filter (thickness 1.6 μm). A few drops of 0.5 M KOH aqueous solution were poured on a glass microfibre filter acting as an electrolyte. Fig. 13 (a-c) presents the CV curves of the CML1, CML2 and CML3 electrodes in a two-electrode system. The CV profiles exhibit nearly rectangular shapes, especially at low scan rates, which is indicative of ideal double-layer capacitance with negligible resistive or faradaic contribution. As the scan rate increases, the area under the curves expands consistently without significant distortion, demonstrating robust capacitive

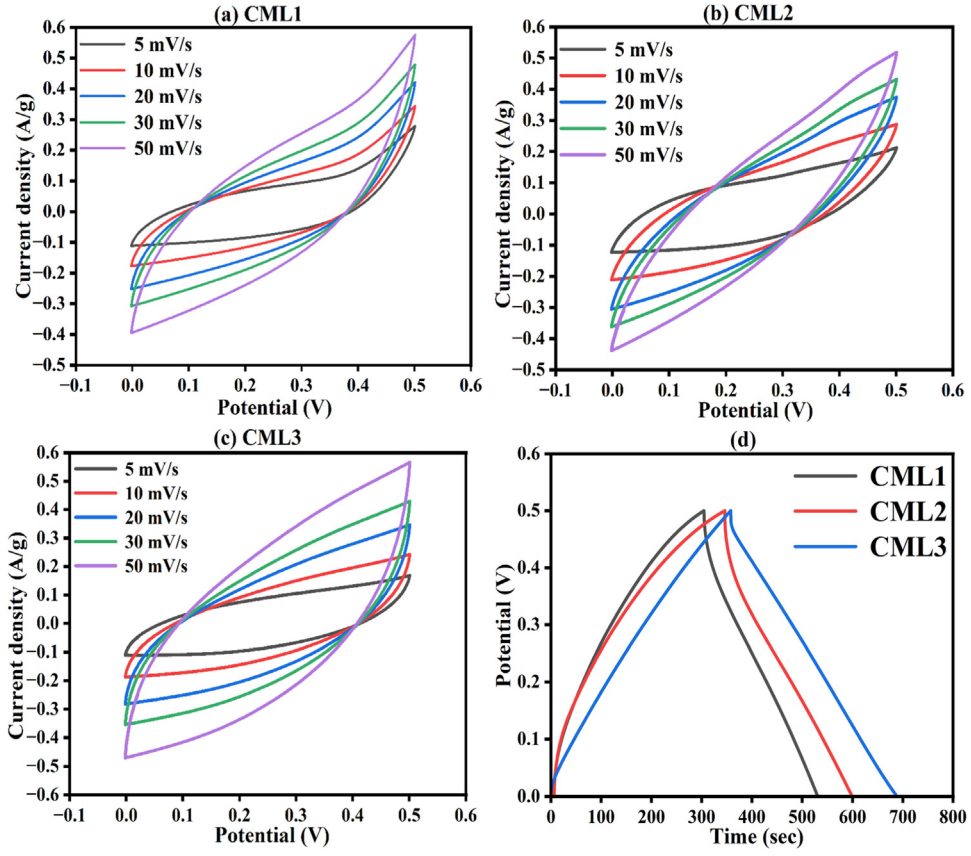

Fig. 13

(a-c) CV curves of the CML1, CML2 and CML3 electrodes in a two-electrode system and (d) GCD curves of the CML1, CML2 and CML3 electrodes in a two-electrode system at a current density of 0.05 A/g.

behaviour and good rate capability. Also, the CV curves of all the electrodes increase from CML1 to CML3 electrodes. Further, the absence of sharp redox peaks across the scan rates suggests that the charge storage is predominantly electrostatic (i.e., EDLC nature), though minor deviations at higher scan rates might hint at limited pseudocapacitive contributions from CML1 to CML3 electrodes (consistent with the results of the three-electrode system). Fig. 13(d) shows the GCD curves of the two-electrode cell of the CML1, CML2 and CML3 electrodes at a current density of 0.5 A/g. All the curves show near-triangular shapes with linear charge/discharge slopes and sharp transitions at the beginning and end of each cycle, indicating high coulombic efficiency and low internal resistance. The following equations were used to calculate specific capacitance (C_p), energy density (E_d) and power density (P_d).

$$C_p = 4\frac{I\Delta t}{m\Delta V} \tag{3}$$

$$E_d = \frac{1}{2}C_p\Delta V^2 \tag{4}$$

$$P_d = \frac{\Delta t}{E_d} \tag{5}$$

where I (A) represents the discharge current and Δt (s) represents discharge time, m represents the mass (grms) and ΔV represents the potential window (V). The Cp values are 90 F/g for the CML1 electrode, 101 F/g for the CML2 electrode and 132 F/g for the CML3 electrode at the current density of 0.05 A/g (Fig. 14a). These values are compared with the literature report given in Table 3. These Cp values demonstrate that the CML3 electrode delivers stable and high-performance electrochemical behaviour, making it a promising candidate for advanced supercapacitor applications. Fig. 14b shows the GCD curves of the CML3 electrode at the current density of 0.05, 0.06, 0.07, 0.08 and 0.09 (A/g) in a two-electrode system. The calculated specific capacitance values

Table 3

Comparative values of specific capacitance with the literature report.

Active electrode	Electrolyte	Specific capacitance	Ref.
CMOF-5–80	H_2SO_4	218	[25]
Porous Carbon	NEt_4BF_4	175	[26]
CZIF69a	H_2SO_4	168	[27]
Cu-MOF	-	135	[28]
Co-MOF	-	129	[29]
PVDF-Bonded Carbon	KCL	74 80	[30]
Co-L/MOF	KOH	74	[31]
CML1		90	Present work
CML2	-	101	
CML2		132	

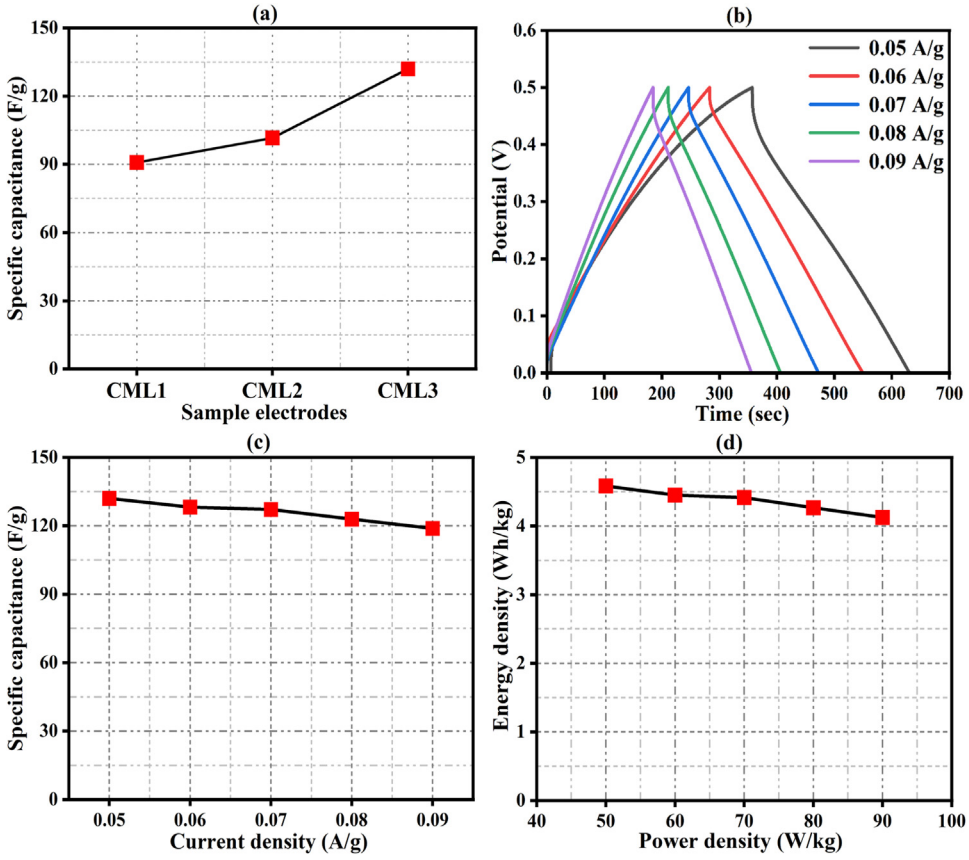

Fig. 14

(a) Specific capacitance of the CML1, CML2 and CML3 electrodes in a two-electrode system, (b) GCD curves, (c) Specific capacitance versus current density and (d) Ragone plot of the CML3 electrode in a two-electrode system.

are 132, 128, 127, 122 and 118 (F/g) at the current density of 0.05, 0.06, 0.07, 0.08 and 0.09 (A/g), respectively (Fig. 14c). The calculated specific capacitance values indicate a gradual decrease in capacitance with higher current density. This determines that at lower current densities, the electrolyte ions have sufficient time to diffuse deeply into the porous framework and access all active sites, leading to higher charge storage. However, at higher current densities, the limited ion diffusion and reduced electrolyte penetration restrict the utilization of active sites, resulting in a lower specific capacitance. This behavior confirms the diffusion-controlled charge storage mechanism in the La-doped CaMo-based MOF electrodes. Fig. 14d shows the Rangone plot of the CML3 electrode. The calculated energy density values are 4.58, 4.45, 4.41, 4.27 and 4.13 (Wh/Kg) at the power density of 50, 60, 70, 80 and 90 (W/Kg). these values determine that at lower power densities, the CML3 electrode allows sufficient time for ion diffusion and full utilization of active sites within the CaMo-doped MOF electrode, resulting in higher energy storage. As the power density increases, the charge–discharge process becomes faster, restricting ion transport and reducing the effective participation of redox-active sites. Consequently, the stored energy decreases, highlighting the trade-off between energy and power densities characteristic of MOF-based supercapacitors. Fig. 15 shows the coulombic efficiency of the CML3 electrode in a two-electrode system. The CML3 electrode retains 96 % efficiency even after 1000 GCD cycles at a current density of 0.1 A/g, determines the stability of the electrode for future generation supercapacitors (last 16 cycles inserted in the Fig. 15).

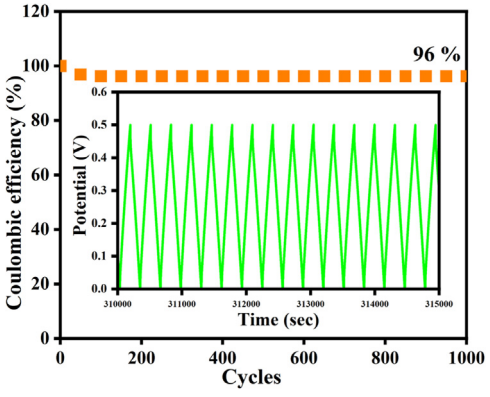

Fig. 15

Coulombic efficiency of the CML3 electrode in a two-electrode system.

5 Conclusion

$La_xCa_{1-x}Mo$-based MOFs were successfully synthesized via a controlled precipitation route and systematically characterized for their structural, morphological, optical and electrochemical

properties. The XRD analysis confirmed the formation of a pure tetragonal scheelite-type $CaMoO_4$ phase (space group $I4_1/a$) without secondary impurities. The average crystallite size of the CML1, CML2, CML3 and CML4 MOFs is 54, 52, 42 and 16 (nm). The SEM and TEM analyses showed a morphological evolution from irregular agglomerates to well-defined rod-like structures, indicating improved crystallinity and directional growth. The increase in the specific capacitance values from CML1 to CML3 electrodes determines the improved charge storage capability and conductivity with La incorporation. Overall, La substitution effectively tailors the structural and functional properties of $CaMoO_4$ MOFs, making them promising candidates for high-performance energy storage and related multifunctional applications.

Declaration of competing interest

The authors declare that they have no known competing financial interests or personal relationships that could have appeared to influence the work reported in this paper.

Data availability

The data that support the findings of this study available from the corresponding author upon reasonable request.

CRediT authorship contribution statement

P. Arularasan: Conceptualization, Data curation, Writing – original draft. **Mohd Arif Dar:** Conceptualization, Data curation, Writing – review & editing. **Mohammad Rezaul Karim:** Formal analysis, Visualization. **P Rajesh:** Methodology, Visualization. **M Pavithra:** Data curation, Validation. **Sambasivam Sangaraju:** Conceptualization, Data curation, Funding acquisition, Writing – review & editing.

Acknowledgement

The authors also appreciate the UAEU_AUA Joint Program 12R248, National Water and Energy Center, United Arab Emirates University.

References

[1] X. Xie, K. Huang, X. Wu, Metal–organic framework-derived hollow materials for electrochemical energy storage, J. Mater. Chem. A. 6 (2018) 6754–6771, doi:10.1039/C8TA00612A.

[2] Z. Chen, et al., Metal–organic framework-derived functional materials for electrochemical energy storage and conversion, Nano. Lett. 20 (3) (2020) 1703614 Article, doi:10.1021/acs.nanolett.0c04898.

[3] Rasu Muruganantham, Yu-Juan Gu, Yi-Da Song, Chung-Wei Kung, Wei-Ren Liu, Ce-MOF derived ceria: insights into the Na-ion storage mechanism as a high-rate performance anode material, Appl. Mater. Today. 22 (2021) 100935 2352-9407, doi:10.1016/j.apmt.2021.100935.

[4] Rasu Muruganantham, Jeng-Shin Lu, Irish Valerie Buiser Maggay, Bor Kae Chang, Po Kai Wang, Wei-Ren Liu, Modification of spinel-based CoV_2O_4 materials through Mn substitution as a potential anode material for Li-ion storage, Surface. Coating. Technol. 389 (2020) 125602 0257-8972, doi:10.1016/j.surfcoat.2020.125602.

[5] A. Tabrizi, et al., A stable dual-function lanthanum MOF: simultaneous CO_2 capture & catalysis, J. CO_2 Utiliz. (2025) 102974, doi:10.1016/j.jcou.2024.102974.

[6] J. Fortune, et al., Chiral lanthanum metal–organic framework with gated CO_2 sorption, J. Am. Chem. Soc. 144 (2022) 1234–1238, doi:10.1021/jacs.2c02351.

[7] Z. Hou, R. Chai, M. Zhang, C. Zhang, P. Chong, Z. Xu, … J. Lin, Fabrication and luminescence properties of one-dimensional $CaMoO_4$: ln^{3+} (Ln= Eu, Tb, Dy) nanofibers via electrospinning process, Langmuir 25 (20) (2009) 12340–12348, doi:10.1021/la9016189.

[8] A.R. Das Neves Stigger, V.F. Hernandes, M.M. Ferrer, M.L. Moreira, Optical and electrical features of calcium molybdate scheelite solar cells, J. Chem. 47 (26) (2023) 12458–12467, doi:10.1039/D3NJ01434G.

[9] P. Patra, K. Jayanthi, F. Margit, S.R. Keshri, S. Bysakh, K. Biswas, … K. Annapurna, The effect of rare earth (RE 3+) ionic radii on transparent lanthanide-tellurite glass-ceramics: correlation between 'hole-formalism'and crystallization, Mater. Advance. 4 (12) (2023) 2667–2682, doi:10.1039/D3MA00036B.

[10] Joop A. Peters, Kristina Djanashvili, Carlos F.G.C. Geraldes, Carlos Platas-Iglesias, The chemical consequences of the gradual decrease of the ionic radius along the Ln-series, Coord. Chem. Rev. 406 (2020) 213146 0010-8545, doi:10.1016/j.ccr.2019.213146.

[11] Qinqin He, Hongjun Zhao, Zedong Teng, Yin Wang, Weiling Sun, Yali Guo, Xiaonan Ji, Wei Hu, Su Shiung Lam, Min Li, Efficient recovery of phosphate by Fe3O4/La-MOF: an insight of adsorption performance and mechanism from electrochemical properties, Sep. Purif. Technol. 314 (2023) 123529 1383-5866, doi:10.1016/j.seppur.2023.123529.

[12] Madappa C. Maridevaru, Aiswarya Konchery, Sanjhana Anandan, Vetriselvi Thirunavukarasu, Abdullah Al Souwaileh, Jerry J. Wu, Sambandam Anandan, Lanthanum-based metal-organic framework nanorods for removal of dye pollutants with machine language predictions, J. Phys. Chem. Solid. 199 (2025) 112580 0022-3697, doi:10.1016/j.jpcs.2025.112580.

[13] F.M. Alzahrani, N.S. Alsaiari, K.M. Katubi, A. Amari, M.A. Tahoon, I.H. Alsohaimi, Synthesis, characterization, and application of magnetized lanthanum (III)-based metal-organic framework for the organic dye removal from water, Adsorption Sci. Technol 2022 (2022), doi:10.1155/2022/3513829.

[14] H.F. Zhai, W. Li, J. Zhang, et al., Excitation-induced tunable luminescent properties of polyhedral $CaMoO_4$ microcrystallites, J. Mater. Sci. 32 (2021) 10008–10017, doi:10.1007/s10854-021-05659-2.

[15] M. Minakshi, D.R. Mitchell, C. Baur, J. Chable, A.J. Barlow, M. Fichtner, … R. Ahuja, Phase evolution in calcium molybdate nanoparticles as a function of synthesis temperature and its electrochemical effect on energy storage, Nanoscale Advance. 1 (2) (2019) 565–580, doi:10.1039/c8na00156a.

[16] H. Zhai, J. Qi, Y. Tan, L. Yang, H. Li, Y. Kang, … H.S. Park, Construction of 1D-MoS_2 nanorods/$LiNb_3O_8$ heterostructure for enhanced hydrogen evolution, Appl. Mater. Today. 18 (2020) 100536, doi:10.1016/j.apmt.2019.100536.

[17] X. Cui, K. Tuokedaerhan, H. Cai, Z. Lu, Effect of annealing temperature on the microstructure and optical properties of lanthanum-doped hafnium oxide, Coatings 12 (4) (2022) 439, doi:10.3390/coatings12040439.

[18] Palanisamy Rajkumar, Vediyappan Thirumal, Akshaya Subhramaniyan Rasappan, Maalavika S. Iyer, Sankaiya Asaithambi, Kisoo Yoo, Jinho Kim, Electrochemically enhanced battery-type Ni substituted CaMo-MOF electrodes: towards futuristic energy storage system, J. Energy Stor. 80 (2024) 110284 2352-152X, doi:10.1016/j.est.2023.110284.

[19] H.F. Zhai, W. Li, J. Zhang, et al., Excitation-induced tunable luminescent properties of polyhedral CaMoO4 microcrystallites, J. Mater. Sci. Mater. Electron. 32 (2021) 10008–10017, doi:10.1007/s10854-021-05659-2.

[20] Zhiyao Hou, Ruitao Chai, Milin Zhang, Cuimiao Zhang, Peng Chong, Xu Zhenhe, Guogang Li, Jun Lin, Fabrication and luminescence properties of one-dimensional CaMoO4: ln3+(Ln=Eu, Tb, Dy) nanofibers via electrospinning process, Langmuir 25 (20) (2009) 12340–12348, doi:10.1021/la9016189.

[21] Titipun Thongtem, Anukorn Phuruangrat, Somchai Thongtem, Characterization of MMoO4 (M=Ba, Sr and Ca) with different morphologies prepared using a cyclic microwave radiation, Mater. Lett. 62 (3) (2008) 454–457, doi:10.1016/j.matlet.2007.05.059.

[22] Mingyue Ma, Haidong Li, Hongwen Zhang, Daocheng Pan, Solution-deposited highly luminescent Eu3+-doped CdMoO4 thin films, J. Lumin. 203 (2018) 702–706 0022-2313, doi:10.1016/j.jlumin.2018.07.023.

[23] X. Zhao, K. Tao, L. Han, Self-supported metal–organic framework-based nanostructures as binder-free electrodes for supercapacitors, Nanoscale 14 (2022) 2155–2166, doi:10.1039/D1NR08284A.

[24] M.R. Biradar, C.R. Rao, S.V. Bhosale, S.V. Bhosale, Flame-retardant 3D covalent organic framework for high-performance symmetric supercapacitors, Energy Fuel. 37 (6) (2023) 4671–4681, doi:10.1021/acs.energyfuels.2c04226.

[25] K. Cendrowski, W. Kukulka, T. Kedzierski, S. Zhang, E. Mijowska, Poly(vinylidene fluoride) and carbon derivative structures from eco-friendly MOF-5 for supercapacitor electrode preparation with improved electrochemical performance, Nanomaterials 8 (11) (2018) 890, doi:10.3390/nano8110890.

[26] S. Jin, H. Deng, L. Zhan, W. Qiao, L. Ling, Synthesis of 3D hierarchical porous carbon as electrode material for electric double layer capacitors, New Carbon Mater 27 (2012) 87–92, doi:10.1016/S1872-5805(12)60005-5.

[27] Q. Wang, W. Xia, W. Guo, L. An, D. Xia, R. Zou, Functional Zeolitic-Imidazolate-framework-templated porous carbon materials for CO_2 capture and enhanced capacitors, Chem. Asian J. 8 (2013) 1879–1885, doi:10.1002/asia.201300147.

[28] A. Zaka, M.W. Iqbal, A.M. Afzal, H. Hassan, S. Alharthi, M.A. Amin, A.M. Saeedi, H.B. Albargi, A. Alhadrami, N.D. Alqarni, M.Z. Ansari, Synergistic innovations in energy Storage: cu-MOF infused with CNT for supercapattery devices and hydrogen evolution reaction, Inorg. Chem. Commun. 159 (2024) 111739 1387–7003, doi:10.1016/j.inoche.2023.111739.

[29] M.A. Dar, S.R. Majid, S. Sarkar, et al., Synthesis and characterization of binder-free Ni, Cu, Mn, and Co metal–organic frameworks for supercapacitors, Ionics (Kiel). 31 (2025) 3715–3726, doi:10.1007/s11581-025-06138-y.

[30] B.-H. Park, J.-H. Choi, Improvement in the capacitance of a carbon electrode prepared using water-soluble polymer binder for a capacitive deionization application, Electrochim Acta. 55 (2010) 2888–2893, doi:10.1016/j.electacta.2009.12.084.

[31] C.M. Hangarter, B. Dyatkin, M. Laskoski, M.C. Palenik, J.B. Miller, M. Tyagi, C.A. Klug, A cobalt-based layered MOF material for supercapacitor applications, J. Energy Stor. 89 (2024) 111476, doi:10.1016/j.est.2024.111476.